AGU PUBLICATIONS

JGR

Journal of Geophysical Research: Oceans

RESEARCH ARTICLE

10.1002/2015JC011459

Wind-wave-induced velocity in ATI SAR ocean surface currents: First experimental evidence from an airborne campaign

Adrien C. H. Martin[1], Christine Gommenginger[1], Jose Marquez[2,3], Sam Doody[2], Victor Navarro[3], and Christopher Buck[4]

[1]National Oceanography Centre, Southampton, UK, [2]Airbus Defence and Space, Portsmouth, UK, [3]Starlab Ltd., Harwell, UK, [4]ESA ESTEC, Noordwijk, Netherlands

Key Points:
- Accurate ATI SAR airborne estimates of wind-wave-induced artifact surface velocity
- Comprehensive remote and in situ data from an airborne campaign
- Validation of an airborne dual-beam high squint (45°), low incidence angle (27°–43°) ATI SAR system

Correspondence to:
A. C. H. Martin,
admartin@noc.ac.uk

Citation:
Martin, A. C. H., C. Gommenginger, J. Marquez, S. Doody, V. Navarro, and C. Buck (2016), Wind-wave-induced velocity in ATI SAR ocean surface currents: First experimental evidence from an airborne campaign, *J. Geophys. Res. Oceans*, *121*, 1640–1653, doi:10.1002/2015JC011459.

Received 25 NOV 2015
Accepted 10 FEB 2016
Accepted article online 13 FEB 2016
Published online 7 MAR 2016

Abstract Conventional and along-track interferometric (ATI) Synthetic Aperture Radar (SAR) senses the motion of the ocean surface by measuring the Doppler shift of reflected signals. Measurements are affected by a Wind-wave-induced Artifact Surface Velocity (WASV) which was modeled theoretically in past studies and has been estimated empirically only once before with Envisat ASAR by Mouche et al. (2012). An airborne campaign in the tidally dominated Irish Sea served to evaluate this effect and the current retrieval capabilities of a dual-beam SAR interferometer known as Wavemill. A comprehensive collection of Wavemill airborne data acquired in a star pattern over a well-instrumented validation site made it possible for the first time to estimate the magnitude of the WASV, and its dependence on azimuth and incidence angle from data alone. In light wind (5.5 m/s) and moderate current (0.7 m/s) conditions, the wind-wave-induced contribution to the measured ocean surface motion reaches up to 1.6 m/s upwind, with a well-defined second-order harmonic dependence on direction to the wind. The magnitude of the WASV is found to be larger at lower incidence angles. The airborne WASV results show excellent consistency with the empirical WASV estimated from Envisat ASAR. These results confirm that SAR and ATI surface velocity estimates are strongly affected by WASV and that the WASV can be well characterized with knowledge of the wind knowledge and of the geometry. These airborne results provide the first independent validation of Mouche et al. (2012) and confirm that the empirical model they propose provides the means to correct airborne and spaceborne SAR and ATI SAR data for WASV to obtain accurate ocean surface current measurements. After removing the WASV, the airborne Wavemill-retrieved currents show very good agreement against ADCP measurements with a root-mean-square error (RMSE) typically around 0.1 m/s in velocity and 10° in direction.

1. Introduction

Conventional and along-track interferometric (ATI) Synthetic Aperture Radar (SAR) provides direct measurements of the motion of the ocean surface based on the detection of anomalous shifts in Doppler frequency or phase. The Doppler Centroid Anomaly (DCA) method, which detects the additional Doppler shift in frequency induced by the motion of the ocean surface, was first demonstrated with airborne and SEASAT satellite data [*Shuchman and Meadows*, 1980; *Rufenach et al.*, 1983]. A few years later, the first high-resolution maps of ocean surface velocity were produced with an airborne along-track interferometry (ATI) system [*Goldstein and Zebker*, 1987; *Goldstein et al.*, 1989]. For an infinite Doppler bandwidth [*Rufenach et al.*, 1983], the DCA estimates of the Doppler shift anomaly (ω_D) is related to the surface radial velocity (u_r) in the line of sight of the radar by $\omega_D = -2u_r.k_e$ with k_e the radar electromagnetic wave number. The principle of the ATI technique is to produce two complex SAR images separated by a sufficiently short time lag (τ) to ensure coherence between the two images. The pixel-to-pixel phase difference between the two images, known as the interferometric phase or interferogram, is related with good approximation [*Graber et al.*, 1996] to the shift in mean Doppler frequency between the Doppler spectra of the two images by $\Delta\phi = \omega_D\tau$. The time lag is related to the platform velocity (V_p) and the baseline distance (B) between the phase centers of the two antennas which produce the two complex SAR images by $\tau = B/V_p$.

Thus, both DCA and ATI techniques measure similar Doppler properties of the backscattered signals, but with important differences. The ATI technique relies on the availability of two SAR images but permits estimation of the radial velocity at very fine spatial resolution, in principle down to the full SAR resolution, whereas the DCA method

operates on a single SAR image but requires averaging over a larger number of SAR image pixel to obtain a smooth Doppler spectra from which to accurately derive the small anomalous Doppler shift due to the surface motion. While there has been renewed interest in DCA following its exploitation with Envisat Advanced Synthetic Aperture Radar (ASAR) data [*Chapron et al*., 2005], here we focus solely on the capability of the ATI technique.

As we have seen, DCA and ATI measurements are sensitive to the surface motion, which consists of many components including those related to the radar response to the surface. The ocean surface motion includes ocean surface currents, the orbital velocity of surface gravity waves and the phase velocity of the scatterers responsible for the backscatter (e.g., Bragg scatterers for moderate to high incidence angles). Hereafter, the velocity components sensed by SAR systems but which are not associated with effective horizontal mass transport will be referred in this paper as Wind-wave-induced Artifact Surface Velocity (WASV).

First observational studies of surface current retrieval with SAR [e.g., *Shuchman and Meadows*, 1980; *Goldstein and Zebker*, 1987] did not attempt to correct for wind and wave impact or [*Goldstein et al*., 1989; *Shemer et al*., 1993] corrected only for the Bragg phase velocity (in L-band $\sim$ 0.5 m/s upwind). The more complex dependence of the Doppler spectrum on surface waves was shown by *Thompson et al*. [1991], *Chapman et al*. [1994], and *Plant* [1997] using various data sets acquired on a fixed platform during the SAXON FPN experiment [*Plant and Alpers*, 1994]. They pointed out the correlation between the long wave orbital velocity and the wave tilt modulation, which affect the SAR backscatter amplitude and therefore the mean Doppler frequency, since the backscatter amplitude weights the contribution of the Doppler frequencies in the Doppler spectrum. This is well illustrated in *Chapron et al*. [2005]. *Graber et al*. [1996] presented comparisons of surface radial velocity from an airborne L-band ATI SAR system and an exemplary in situ validation setup including shipboard ADCP, HF radar, weather buoys, and directional wave buoys. *Graber et al*. [1996] gave an estimate of the wind-wave contribution measured by the airborne ATI as a function of incidence angle for a specific azimuth direction (55° off the downwind direction). The estimate was found to be consistent with the *Thompson et al*. [1991] theoretical model for two wind directions separated by 15°. *Fois et al*. [2015] presented also some early measurements from the fixed SAXON FPN platform experiment, but the data were only available for high incidence angles (50° and 60°) and showed large spread.

Since these first observations, a large number of theoretical models have been developed [e.g., *Toporkov and Brown*, 2000; *Romeiser and Thompson*, 2000; *Gelpi and Norris*, 2003; *Mouche et al*., 2008; *Nouguier et al*., 2011; *Hansen et al*., 2012; *Fois et al*., 2015] but except for the last two, these models have received little or no validation against observations. *Mouche et al*. [2012] provide the first and only empirical model of the WASV, derived from global estimates of the Doppler shift anomaly in Envisat ASAR data evaluated against ECMWF model winds as ground truth. Unfortunately, the Envisat ASAR data used to develop the *Mouche et al*. [2012] empirical model present a wide spread in Doppler frequency ($\sim$7 Hz) equivalent to radial velocity errors $\sim$35 cm/s at 30° of incidence angle. These could be due to both the low accuracy of the Doppler shift anomaly derived from Envisat ASAR [*Hansen et al*., 2011] and uncertainties about the ECMWF model wind estimates.

The aim of this paper is to quantify, based on measurements alone, the magnitude of the WASV, and its dependence on azimuth and incidence angle as observed during an airborne campaign. The airborne data were acquired using a dual-beam ATI SAR system known as Wavemill during the Wavemill proof-of-concept (PoC) experiment that took place in October 2011 in Liverpool Bay off the west coast of the Great Britain (United Kingdom). The airborne data are supported by a comprehensive set of in situ measurements used to characterize the geophysical conditions during the flights. The airborne results are then compared with the empirical WASV model derived from Envisat ASAR data [*Mouche et al*., 2012].

Section 2 will present the experimental data, with first a brief description of the airborne system, then the campaign overview and finally the geophysical conditions during the flights. Section 3 presents the Wavemill results, which will be discussed in section 4. Summary and conclusions can be found in section 5.

2. Experimental Data

2.1. Wavemill Airborne Proof-of-Concept System

2.1.1. System Description

The Wavemill airborne system was developed and deployed by Astrium UK (now Airbus Defence and Space UK) as a prototype demonstrator of the Wavemill satellite mission concept presented in *Buck* [2005] in the

Figure 1. (left) Douglas DC-3 aircraft used during the Wavemill proof-of-concept campaign, showing the Wavemill antennas inside the radome. The radome transparency is the result of photomontage. (right) Zoom on the two mounted Wavemill antenna pairs. The gimbal appears in black and connects the aircraft and the antenna system. Note the 50 cm physical baseline between each pair of antenna, as well as the squinted orientation of the antennas.

context of a project funded by the European Space Agency. Only the main system characteristics are summarized here, with full details provided in the Wavemill proof-of-concept final report [*Wavemill PoC Team*, 2012]. The Wavemill system is composed of two pairs of antennas, looking in pairs 45° fore and 45° aft with respect to the aircraft broadside. The system operates at X-band (9.55 GHz) with a bandwidth of 100 MHz and transmits and receives using vertical polarization (VV). For each pair of antennas, only one antenna operated in transmit/receive mode (monostatic channel), while the second operated in receive mode only (bistatic channel). The physical baseline between each pair of antennas was 50 cm. The system was set up on a Douglas DC-3 aircraft (Figure 1) and the aircraft velocity (V_p) during the flights varied between 70 and 85 m/s, leading to a time lag (τ) between the two antenna pairs of about 3 ms which is short enough to ensure signal coherence between the two complex SAR images.

The antenna beam width was 30° in elevation and azimuth. The aircraft altitude was approximately 2790 m, giving a swath width of about 1800 m and incidence angles varying from 24° (near range) to 45° (far range).

The aircraft featured an inertial motion unit/global positioning system (IMU/GPS C-Migits CMG-310 manufactured by BEI Systron Donner) and a differential GPS (DGPS Cresent R110 manufactured by Hemisphere) to provide navigation and attitude data. The attitude/position data were reported at 100 Hz. The accuracies at 1 sigma were 0.1 m/s for horizontal and vertical velocity, 0.06° for roll and pitch and 0.09° for heading. The antenna system was mounted on a gimbal (FLIR D48E) pointing at 26.6° incidence on the left-hand side of the aircraft. The gimbal compensated for the aircraft motion at a 10 Hz rate by step of 0.013° in roll and yaw but did not compensate for pitch variation. The mounted system on the Douglas DC-3 aircraft is shown in Figure 1 (right).

2.1.2. ATI SAR Processing

The single look complex (SLC) images were produced with a ground range resolution between 5.3 m at near range (24°) and 1.5 m at far range (45°). The azimuth resolution is 1.06 m. The SAR focusing is processed to acquisition Doppler (AD) geometry [*Bara et al.*, 2000; *Fornaro et al.*, 2002] with a bandwidth of 75 Hz. As the processing is done over lines of constant Doppler frequencies, the squint angle on the ground varies across the swath. The squint angle is ±65° at near range (24° incidence angle), ±45° at midrange (32°) and ±32° at far range (45°). A direct backprojection algorithm [*Ulander et al.*, 2003] was used for target focusing and to correct the effect of the residual attitude motion not compensated by the gimbal. Indeed, the attitude motion can introduce an across-track interferometric (XTI) baseline, which would introduce a phase sensitivity to a flat surface (and to a lesser extent to the surface topography).

The interferogram $\Delta\phi_j$ is a pixel-to-pixel phase difference between the two complex SAR images computed as

$$\Delta\phi_j = \arg\{M_j.S_j^*\}, \qquad j=1,2 \tag{1}$$

and the coherence γ_j is defined as

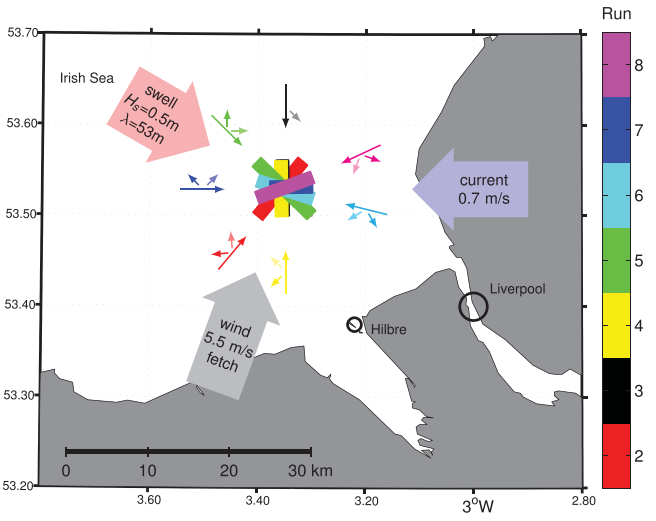

Figure 2. Location of Wavemill airborne proof-of-concept data over the 7 × 7 km Mersey Bar Light (MBL) area in the Liverpool Bay off the west coast of the UK. Each run is represented with a different color. For each run, the colored long arrow represents the aircraft flight direction and the two small arrows represent the line-of-sight direction of the fore (pale color) and aft (bright color) pairs of antennas. The position of Liverpool city and Hilbre Island has been indicated by black circles. The large wide arrows summarize the geophysical conditions for current, wind, and swell.

$$\gamma_j = \frac{|M_j . S_j^*|}{\sqrt{|M_j|^2 . |S_j|^2}}, \qquad j = 1, 2 \qquad (2)$$

where M and S refer to the SLC images of the master or slave antenna of each antenna pair and the subscripts ($j = 1$) and ($j = 2$) represent, respectively, the fore and aft-looking antenna pairs.

The interferometric phase was absolutely calibrated for one run using land as a static target, over which the interferometric phase was set to zero. For runs over water, the calibration target was the Mersey Bar Light (MBL) buoy, a permanently moored 38 m long vessel, which was assumed to be suitably static. The interferometric phase varied slightly from run to run, within a spread of ±0.1 rad, equivalent to an uncertainty in radial velocity of about 0.15 m/s.

The SAR amplitude was not calibrated, so there were amplitude differences between the SLC from the fore and aft-looking antennas. This means no calibrated normalized radar cross section (NRCS) products were available, which is unfortunate since it would have permitted the retrieval of wind speed using a standard geophysical model function [e.g., *Hersbach et al.*, 2007].

2.2. Airborne Campaign Overview

The Wavemill proof-of-concept campaign was carried out in the last week of October 2011 over various sites in the Irish Sea off the west coast of the Great Britain (United Kingdom).

Two scientific flights took place over 2 days. In this paper, only the data acquired on 26 October 2011 are presented. All data were acquired within 70 min of each other between 00:19UTC and 01:27UTC during the maximum ebbing tidal flow (∼0.7 m/s westward). The instrument was operated in the so-called "Javelin" configuration, corresponding to an antenna configuration with a pure along-track physical baseline. The along-track separation was 50 cm (no across-track separation) between each pair of antennas.

The data acquisitions considered in this paper are represented in Figure 2, showing the "star pattern" of seven runs with seven heading directions, centered over the Mersey Bar Light (MBL) buoy where in situ current and wave measurements were available. The figure shows the segments of Wavemill data acquired over a 7 × 7 km square centered on MBL. Data for each run are identified by a given color, with the long arrow representing the flight direction of the aircraft and the two small arrows represent the line of sight of the fore-looking and aft-looking pairs of antennas. Note that, for run R3 (black), only data acquired for the fore-looking antenna pair were available (the data from the aft-looking antenna pair being corrupted).

2.3. Geophysical Conditions and In Situ Validation Data

The geophysical conditions during the airborne campaign are summarized in Figure 2 and were estimated thanks to various in situ data at MBL and other local observations. It is assumed that the in situ data at MBL are representative of the conditions over the whole 7 × 7 km area. While the bathymetry over the area is relatively shallow (∼20 m), it is also reasonably uniform.

Ocean current information was available from both Acoustic Doppler Current Profiler (ADCP) and HF radar. The ADCP was deployed on a sea bed-mounted frame in 23.5 m water depth close to the MBL. Ocean surface currents were taken from the ADCP near-surface vertical bin located approximately 19.7 m above the

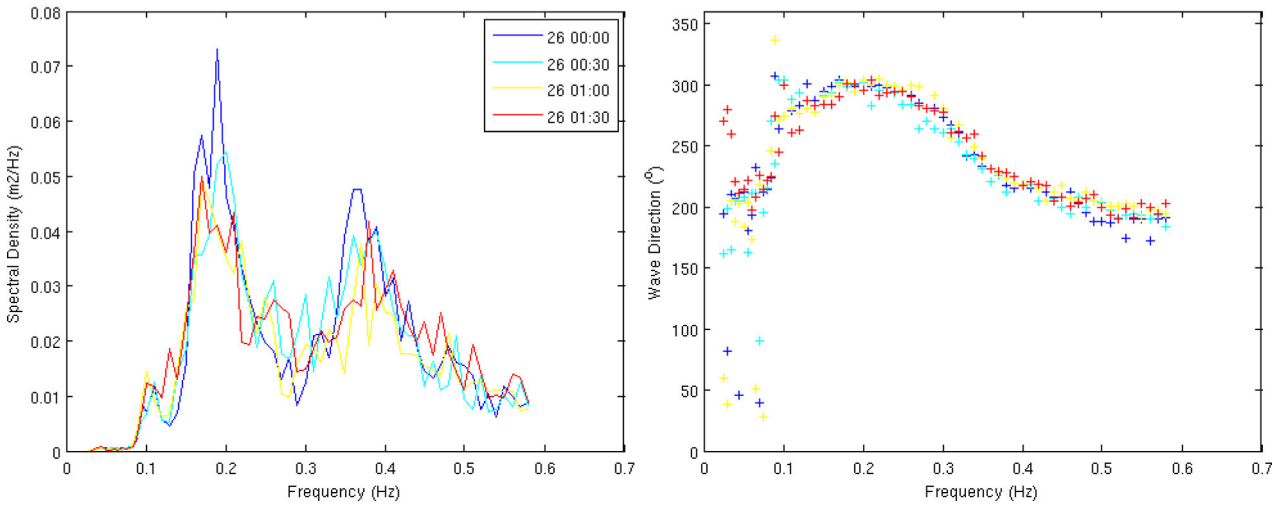

Figure 3. (left) Wave spectral density measured at Mersey Bar Light (MBL) every 30 min during the airborne runs over MBL, showing the bimodal nature of the sea state. (right) Wave direction at each frequency, showing the swell peak (~0.17 Hz equivalent to 53 m wavelength) from 300°, the wind peak (~0.4 Hz) from 230°, and the shortest wind waves from 200°.

seabed, corresponding to between 4 and 2 m below the surface as the tide fell. The ADCP gives measurements every 10 min, with a reported accuracy of ~0.01 m/s.

A WERA HF radar system also monitored currents over the MBL area, operating at 12–16 MHz that correspond to a Bragg wavelength of 12–9 m. Surface currents and Bragg wave direction are reported every 20 min, averaged over 9 min and cells of 4 × 4 km. The reported accuracy is better than ~0.05 m/s.

During the acquisition of the star pattern runs, the current was westward with a maximum ebb flow of 0.7 m/s. Both ADCP and HF radar measurements indicated a stable westward current during that time. The average ([minimum, maximum]) surface current values measured by the ADCP were equal to 0.72 ([0.68, 0.77]) m/s flowing to 272° ([267°, 275°]), and for the HF radar cell closest to MBL, to 0.73 ([0.66, 0.76]) m/s flowing to 288° ([285°, 289°]). The difference between the HF radar and ADCP surface current vectors (HF minus ADCP) has a magnitude of 0.20 m/s flowing to 7°. This value is about 3–4% of the wind speed (5.5 m/s from the South; see information on wind below) and could be linked to wind and Stokes drift that is known to affect HF radar current data [e.g., *Ardhuin et al*., 2009].

No in situ wind data were available at MBL. Measurements from a coastal weather station at Hilbre Island (53.38°N 3.22°W) reported winds between 4.8 and 5.5 m/s from the south (180°). Wind speed estimates from the Oceansat-2 scatterometer 12.5 km resolution products reported winds closest to MBL on the 26 October 2011 at 00:15 to be around 5–6 m/s from a southerly direction, which is broadly consistent with the wind conditions measured at Hilbre Island.

Directional wave spectra were measured by the directional wave buoy at MBL operated by CEFAS (Centre for Environment, Fisheries and Aquaculture Science). The buoy reports double-peaked spectra, where the main spectral peak is associated with a weak swell system ($H_s = 0.5$ m, $\lambda = 53$ m) travelling into the area from the North-West (Figure 3). Since the area is characterized by shallow bathymetry (~20 m), some shoaling of the longer swell waves may be occurring.

The secondary peak in the spectrum (Figure 3) indicates shorter wind waves ($\lambda \approx 10$ m) travelling into the area from 230°. The shortest ocean gravity waves reported in the spectrum are around 5 m wavelength travelling from 200°. The slight difference in direction between the wind-sea peak and these short waves is probably due to the limited fetch south of MBL because of nearby land. Both wave directions at MBL differ also slightly from the wind direction measured by the coastal weather station at Hilbre Island. However, since the weather station is located on land at the mouth of the river Dee, the wind direction it reports may not be representative of the wind direction at MBL. The wind direction suggested by the shortest waves in the spectrum at MBL (200°) is considered to give the best indication of the wind conditions at MBL.

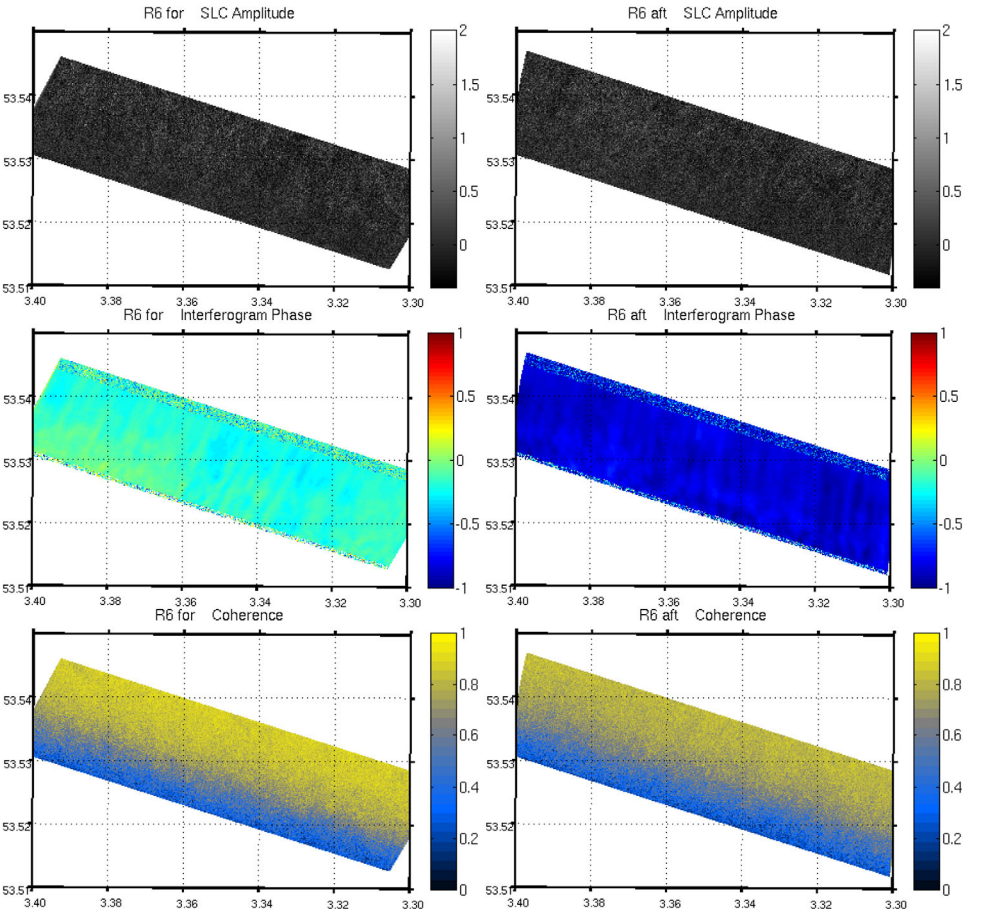

Figure 4. Wavemill airborne demonstrator measurements for run R6 showing (top) normalized amplitudes corrected for incidence angle dependence (arbitrary unit), (middle) interferograms (rad), and (bottom) coherence, obtained over the 7 × 7 km area over MBL for (left) fore-looking and (right) aft-looking antennas. On each figure, coordinates are longitude and latitude. The flight goes from nearly East to nearly West with the system looking on the left, so that the near range part of the scene is located further north than far range. Data have been averaged on 5 × 5 m grid cells. The low frequency long-crested oscillations seen in the interferograms affect all incidence angles and are associated with residual platform attitude errors.

3. Results

3.1. Example Wavemill ATI SAR Data

Figure 4 shows an example of Wavemill amplitude images, interferograms, and coherence maps obtained for the fore-looking and aft-looking pairs of antennas for run R6 after averaging over 5 × 5 m grid cells. Run R6 flew in an almost East-to-West direction, with the system looking on the left of the aircraft. Amplitudes were corrected for decay with range using the median along track.

The Wavemill amplitude images (top) and coherence map (bottom) do not display strong inhomogeneity or features, unlike the interferograms (middle). Two bands of random values in the interferograms at very near and very far ranges are processing artifacts that were removed from the analyses. Data with incidence angles between 26.4° and 43.9° were kept for all runs. The oscillations observed in the interferograms are due to residual uncorrected attitude effects to which the Wavemill system is very sensitive (as reported also by e.g., *Hwang et al.* [2006]). The along-track variability in the interferograms differs between runs and is smaller at near range (by about half) than at far range. Because of the presence of strong outliers in the data, the variability in the data is expressed with the interquartile range (iqr) rather than the standard deviation. The iqr of the along-track oscillations of the interferometric phase is below 0.2 rad for all runs except run R2 for which it ranges between 0.2 and 0.25 rad at far range. The coherence maps highlight the loss of coherence from near range to far range linked to the rapid reduction in amplitude signal-to-noise ratio with increasing incidence angles.

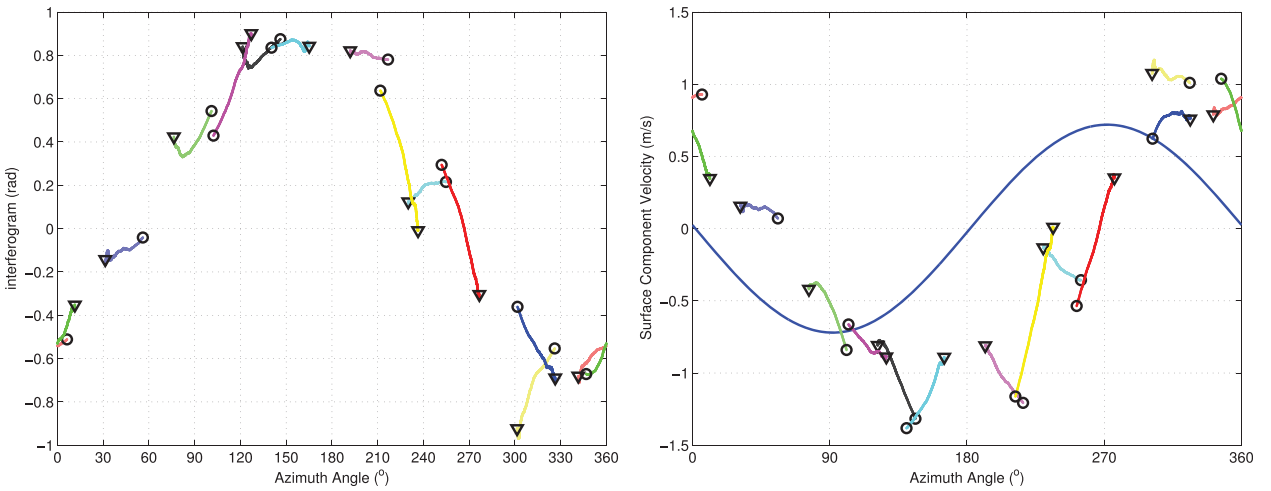

Figure 5. Dependence on azimuth look angle for all runs in the star pattern of the (left) median interferometric phase and (right) median surface velocity at all incidence angles. The circles (triangles) represent the near (far) range for each run. The color code is the same as in Figure 1 with bright colors representing the data for the aft-looking antenna pair and pale colors representing data for the fore-looking antenna pair. The blue curve in (right) represents the projected component of the sea surface current as measured by the ADCP (westward ebb flow) at every azimuth angle. An azimuth angle of zero "0" represents geographical North.

3.2. Wind-Wave-Induced Artifact Surface Velocity (WASV)

In this section, the azimuth variation of the Wavemill velocity measurements is examined. For each run, the median value of the interferogram was computed along track at every incidence angle to mitigate the along-track variability in the Wavemill measurements attributed to residual platform attitude effects. No averaging was performed in the cross-track direction so as to retain information about the retrieved velocity with range and incidence angle. For each run, the median interferogram is estimated separately for the fore-looking and aft-looking antenna pair.

Figure 5 (left) represents the median interferogram for each run and each fore-looking and aft-looking antenna pair, plotted as a function of the azimuth look direction with respect to North using oceanographic convention. The colors for each run in Figure 5 are the same as in Figure 2, with bright (pale) colors representing the data obtained with the aft (fore) antenna pair, respectively. The near and far range ends of the median interferogram are indicated as circles and triangles, respectively.

The main feature of these results is a strong sinusoidal variation with a peak in the 160°–340° direction. This azimuth variation is hard to interpret directly in geophysical terms, as it contains the WASV, the surface current and the Wavemill sensitivity to incidence angle. However, it can be noted that for a same incidence angle and azimuth direction, different runs and antennas show similar values of interferometric phase, providing confidence in the quality of the Wavemill airborne data.

The radial surface velocity, u_{surf}, is derived from the radial velocity in the radar line of sight (u_r) or the interferogram as [e.g., *Graber et al.*, 1996]

$$u_{surf} = \frac{u_r}{\sin\theta} = -\frac{V_p}{k_e B}\frac{\phi_j}{\sin\theta} \approx -\frac{0.7\phi_j}{\sin\theta} \tag{3}$$

with k_e the radar wave number, V_p the aircraft velocity (taken as the average value for each run), B the physical baseline, and θ the incidence angle.

Since this transformation invokes the incidence angle through the projection of the line-of-sight velocity onto the surface, it does not affect the values at low and high incidence angle equally, and this changes significantly the dependence of the Wavemill surface velocity on azimuth. This is shown in Figure 5 (right) where the radial surface velocity still shows a strong sinusoidal behavior although with a peak magnitude of almost 1.5 m/s around 180° in azimuth. However, the radial surface velocity plotted in Figure 5 (right) still contains the WASV and the surface current. Here since the surface current is known (for example from in situ ADCP measurements), it is possible to estimate the WASV as the residual velocity after the ADCP surface current is removed from the Wavemill surface velocity measurements.

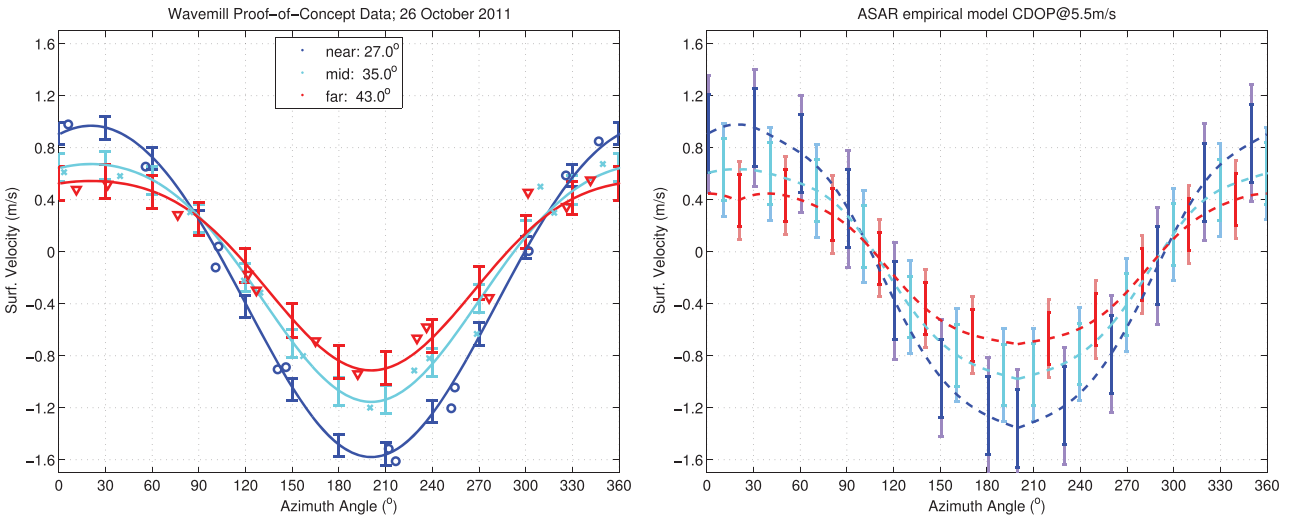

Figure 6. Wind-wave-induced Artifact Surface Velocity (WASV) as a function of azimuth look angle derived from the (left) Wavemill airborne proof-of-concept measurements and (right) the C-DOP Envisat ASAR empirical model [*Mouche et al.*, 2012] for the same geophysical conditions as experienced during the flight. (left) The WASV is calculated as the measured surface velocity minus the ADCP current. Circles, crosses, and triangles represent the Wavemill WASV at near, mid, and far range and are plotted in blue, cyan, and red, respectively. The corresponding curves represent the fitted surface (see equation (4)) for the given incidence angle. The error bars are set by the RMS difference between the fitted curve and the data at the given incidence angle. (right) The WASV is obtained by computing the C-DOP estimates for a wind of 5.5 m/s from 199.8° at the same three incidence angles as shown in Figure 6 (left). The error bars represent the uncertainty (spread) associated with a 5 Hz (7.5 Hz) Doppler anomaly [*Hansen et al.*, 2011; *Mouche et al.*, 2012] projected as a surface velocity uncertainty (spread) at the incidence angles shown.

The blue curve in Figure 5 (right) represents the azimuth dependence of the ocean surface current measured by the ADCP (0.7 m/s at 272°). In Figure 6 (left), we show the WASV obtained by subtracting the blue curve (in Figure 5 (right)) from the Wavemill surface velocity data (in Figure 5 (right)). The Wavemill WASV in Figure 6 (left) is shown only for three incidence angles (27°, 35°, and 43°) in order to reveal also the dependence of the WASV on incidence angle.

The WASV shows a strong sinusoidal dependence on azimuth, with an amplitude that decreases with increasing incidence angle. The maximum value of the WASV is found around 200°, corresponding to the upwind direction. At 27° incidence, the amplitude of the WASV upwind reaches 1.6 m/s, while at 43° incidence, it is around 0.9 m/s. In the downwind direction, around 20°, the magnitude of the WASV is slightly smaller than in the upwind direction. In absolute value, the upwind/downwind ratio is about 1.6–1.7. The magnitude of the WASV is smallest in the crosswind direction.

The data in Figure 6 (left) were fitted with a second-order harmonic function of azimuth direction, i.e.:

$$u_{surf,wind}(\theta,\varphi)=A_2(\theta)+B_2(\theta).cos(\varphi)+C_2(\theta).cos(2\varphi) \quad (4)$$

where A_2, B_2, and C_2 are quadratic functions of incidence angle of the form $A_2(\theta)=a_0+a_1.\theta+a_2.\theta^2$ and the coefficients a_0, a_1, and a_2 are defined in Table 1.

The fitted surface (for incidence angles between 26.4° and 43.9°) explains 97% of the variance of the data with a RMS (root-mean-square) error of 0.11 m/s. The RMS error is slightly better at low incidence angle (<0.09 m/s) and increases with incidence angle (~0.13 m/s at 43.9°). These RMS values are indicated as error bars in Figure 6 (left). The maxima of the fitted harmonic are observed at azimuth angles of 200° and 20° in very good agreement with the upwind and downwind directions. The absolute maximum is observed in the upwind direction.

Table 1. Polynomial Coefficients of the Quadratic Functions of Incidence Angle (θ) Defined in Equation (4), of the Form $A_2(\theta)=a_0+a_1.\theta+a_2.\theta^2$

	0	1	2
a	−1.052	0.04187	−0.0004458
b	−3.77	0.129	0.001356
c	0.4614	−0.02937	0.0003752

Similar analyses applied to amplitude and coherence data (Figure 7) also reveal second-order harmonic variations with azimuth, with maxima in the upwind direction. As expected, the coherence follows the same behavior with azimuth as the amplitude that controls the SNR.

The WASV estimated with the Wavemill airborne proof-of-concept data was compared with estimates from the Envisat

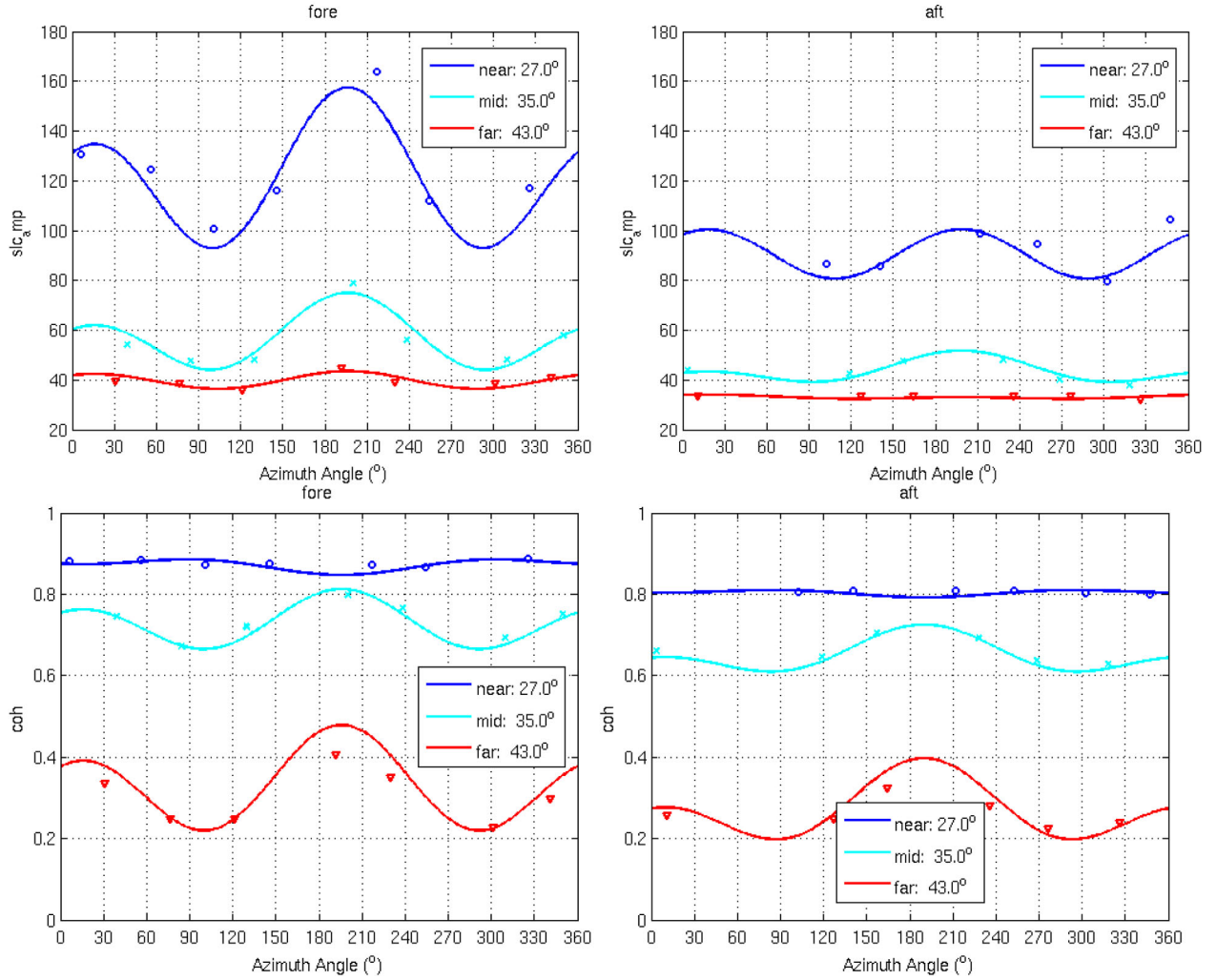

Figure 7. Dependence on azimuth look angle for all runs in the star pattern of the (top) Wavemill normalized amplitude and (bottom) coherence. (left) For the fore-looking antennas. (right) For the aft-looking antennas.

ASAR empirical model by *Mouche et al.* [2012] (known as C-DOP) obtained for a wind speed of 5.5 m/s and a upwind direction of 200° (Figure 6 (right)). To the best of our knowledge, this is the only empirical model available to estimate the WASV. There is a very good agreement between the WASV estimated from the Wavemill data and the empirical model results, both in the form of the azimuth variation, the magnitude of the WASV contribution and in the decrease of the effect with incidence angle. The amplitude of the WASV in the Wavemill PoC data is slightly higher in the upwind direction than for C-DOP but remains within the spread of the C-DOP error bar. This level of agreement is remarkable since the Wavemill data were obtained at X-band with an airborne ATI SAR system, whereas the C-DOP results correspond to an empirical model derived from C-band spaceborne conventional SAR.

3.3. Performance of the Surface Current Vector Measurements

Figure 8 shows the retrieved current vectors for all runs (except R3) over the 7 × 7 km MBL area with a ∼300 × 300 m grid spacing. Run R3 was omitted because the data from the aft-looking antenna pair were corrupted. To improve readability, the data in Figure 8 were subsampled from the original current vector map that has a spatial resolution of 100 × 100 m, where each current measurement is based on ATI SAR data from about 2000 to 6000 pixels depending on range. The figure shows the surface current vectors obtained after correction for the WASV contribution (according to the results in Figure 6 (left) and Table 1) and after combination of the radial velocity estimated from the fore-looking and aft-looking antenna pairs in each run.

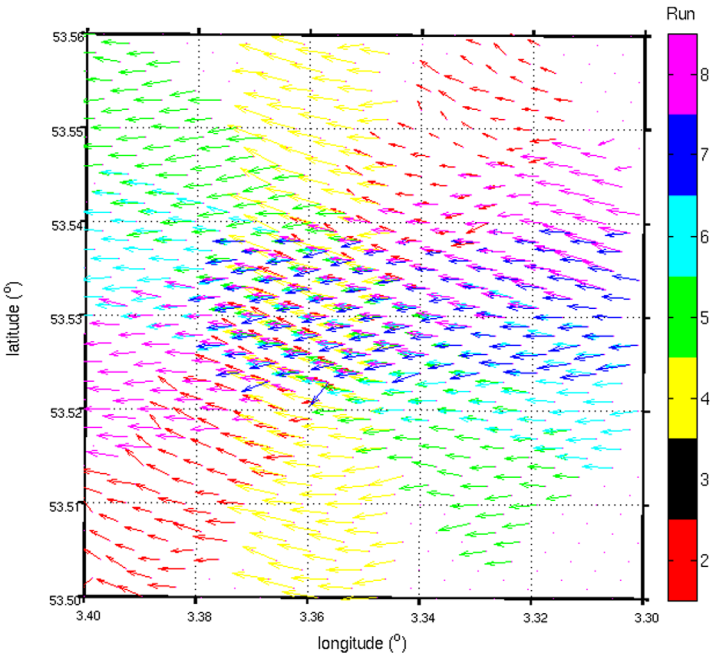

Figure 8. Retrieved surface current vectors for all airborne Wavemill runs (except R3) over the 7 × 7 km^2 MBL area. The data are shown with a ~300 × 300 m grid spacing after subsampling to improve readability. The spatial resolution of the current vector map is 100 × 100 m, where each current measurement is based on ATI SAR data from about 2000 to 6000 pixels depending on range. The data for each run are represented with the same color as in Figure 2. The average retrieved current speed and direction are 0.74 m/s and 274°. R3 was omitted because the data from the aft-looking antenna pair were corrupted.

Figure 8 shows the very good consistency of the current vector fields obtained for different runs, which all display a generally coherent westward current of quasi-uniform magnitude. In the overlapping sections of the runs near the center of the MBL area, there is very good agreement in current magnitude and direction with a spread in direction typically below 10°. The spread in direction is bounded by R7 (slightly more southward) and R2 and R8 (slightly more northward). The largest number of anomalies from the generally westward flow is seen for runs R2, R4, and R7.

Table 2 shows the performance of the retrieved current in terms of mean bias against the ADCP data, standard deviation (std) and root-mean-square error (RMSE) for each run and averaged over all runs. Table 2 highlights the large bias in velocity for R2 and R4 (respectively −0.19 and +0.23 m/s). For all other runs, the velocity bias is less than 0.05 m/s (5 cm/s). The bias in direction is typically less than 6°, except for R2 (12°). The standard deviation (std) and root-mean-square error (RMSE) represent the variability within each run (intrarun), which are typically less than 0.1 m/s and 10° for velocity and direction, respectively, except for R2 and R4.

4. Discussion

These results from the airborne Wavemill PoC campaign confirm the very significant impact of the WASV on direct Doppler measured velocity from SAR and ATI systems. The magnitude of the wind-wave artifact velocity, for the light wind geophysical conditions encountered here, is over twice the magnitude of the tidal ebb flow. However, the very good agreement between the Wavemill measured WASV and the C-DOP empirical model is encouraging as it shows that knowledge of the wind vector could be sufficient to correct for this effect.

Table 2. Performance of the Airborne Wavemill-Retrieved Current Against the ADCP in Terms of Bias, Standard Deviation (std) and Root-Mean-Square Error (RMSE) for Each Run and Averaged Over All Runs[a]

		Velocity (m/s)			Direction (°)		
Run Number	Number of Samples	Bias	std	RMSE	Bias	std	RMSE
2	1438	−0.19	0.13	0.23	12	14	19
4	1131	0.23	0.10	0.25	6	8	10
5	1335	0.05	0.09	0.11	−3	6	7
6	1176	0.02	0.07	0.07	−2	5	5
7	846	0.02	0.08	0.08	−6	7	10
8	1262	0.01	0.09	0.09	3	6	6
All	7188	0.02	0.16	0.16	2	11	11

[a]The statistics were computed for the retrieved current to a 100 × 100 m grid spacing over the 7 × 7 km MBL area shown in Figure 8.

Conversely, the detection of geophysical wind-wave effects in the Wavemill data in agreement with the C-DOP model provides confidence about the very good quality of the airborne Wavemill PoC data set, despite the known challenges of obtaining accurate interferometric SAR measurements from an airborne platform. In addition, the experiment validates for the first time the dual-beam interferometry concept for a high squint angle (45°) and relatively low incidence angle (27°–43°) compared to other examples [e.g., *Frasier and Camps*, 2001; *Farquharson et al*., 2004; *Toporkov et al*., 2005] where systems usually operate with squint angles of 20° and boresight incidence angles above 60°.

We note that the WASV estimated from the satellite-derived C-DOP model show slightly lower amplitude in the upwind direction than the airborne Wavemill WASV. This could be linked to several factors. The C-DOP model represents the average behavior of a large globally distributed spaceborne data set obtained over the open ocean, which shows a large spread in Doppler frequency. In contrast, the airborne Wavemill WASV was obtained in atypical geophysical conditions of opposing current, wind and swell, in a coastal location with relatively shallow waters and limited fetch. The stronger upwind/downwind asymmetry seen for Wavemill could thus be due to the developing wind waves or to wind-wave/current interaction. The impact of the fetch on the WASV could not be examined in this study but needs to be investigated in the future.

The difference in microwave frequency between the C-band C-DOP model (5.5 GHz) and the X-band Wavemill PoC (9.5 GHz) seems to have little impact. Indeed, in this small range of microwave frequencies (centimeter wavelength), the surface Bragg scatterers responsible for the electromagnetic backscatter signal will be of similar scales, and will be sensitive to the same range of wave orbital velocity, facet tilt modulation, and Bragg phase velocity effects.

The Wavemill PoC and C-DOP WASV estimates are obtained for surface velocity measured using two different techniques (resp. ATI and DCA). Using a theoretical model, *Graber et al*. [1996] has shown the difference in precision between the two techniques is less than about 10% of the current speed. More recently, comparison between DCA and ATI using Tandem-X satellite data [*Romeiser et al*., 2014] did not highlight a strong difference in performance between these techniques when multipixel averaging is applied. However, we cannot discount the possibility that this difference in technique could contribute to the differences in WASV amplitude in the upwind direction for Wavemill PoC (ATI) and C-DOP (DCA). Further investigations need to be carried out to assess in more depth the performance and differences between ATI and DCA.

In this experiment, the Wavemill WASV is dominated by the wind effect. The WASV is aligned in the wind direction (200°) and not in the wind-sea peak direction (230°), which suggests a dominant effect of the Bragg scatterers over the wave orbital azimuth variability. There is no perceptible impact of the swell in our data (from North-West, Hs = 0.5, 53 m wavelength). This could be due to the very low energy of the swell system during this experiment. It has been suggested that the impact of swell is nonnegligible [e.g., *Romeiser et al*., 2014] and further airborne campaigns in a well-instrumented site, exposed to high energy swell, are needed to acquire experimental evidence and better understand and quantify the full impact of swell on the WASV.

Our results are in broad agreement with earlier airborne ATI observations obtained in a single broadside direction. *Graber et al*. [1996] estimate the WASV using an airborne L-band SAR ATI system but for a single azimuth look direction. The azimuth look direction was 55° from the downwind direction with a wind speed of 5–6 m/s. The WASV is found to be slightly less than 0.3 m/s and quasi-constant with incidence angle. For an azimuth look direction of 55° from downwind (20° ± 55° = 75°, 325°), the Wavemill PoC WASV gives a value between 0.4 and 0.5 m/s, with very weak dependence on incidence angle. The low sensitivity to incidence angle at this azimuth angle is in good agreement with *Graber et al*. [1996] but the amplitude of the Wavemill WASV is slightly larger than expected (but still within the error bars). With the Bragg phase velocity significantly larger at L-band (0.5 m/s) than X-band (0.2 m/s), one would have expected the opposite. However, it is possible that a slightly stronger tilt modulation effect in X-band could contribute to the larger WASV observed with the X-band Wavemill data.

To estimate the WASV, the current measured by ADCP was removed from the Wavemill measurements. The ADCP measures the Eulerian current at 2–4 m depth. This current is composed of the sum of the tidal current, the wind-induced current at that depth, the Stokes drift at that depth, plus any other Eulerian coastal currents (e.g., inertial currents). The surface currents not captured by the ADCP thus include the wind-induced and Stokes drift at the surface. Part of the WASV therefore includes these currents, so that

correcting SAR and ATI measurements with the empirical WASV will remove these contributions from the measured currents. The HF radar is thought to include a filtered Stokes drift [e.g., *Ardhuin et al*., 2009] and could be used as truth instead of the ADCP. However, as the HF radar filtered Stokes drift depends on the HF radar frequency, it would have made the WASV HF radar frequency dependent. Besides, more recent validation of HF radar currents suggests that HF radars are not sensitive to Stokes drift and also measure Eulerian currents only [*Röhrs et al*., 2015].

Our results illustrate the very good mapping and current retrieval capabilities of the airborne Wavemill instrument over MBL. After removing the WASV, the retrieved currents from different runs reveal a generally coherent westward flow (Figure 8) that is in very good agreement with the ADCP measurements. All runs report an RMSE (root-mean-square error) around or below 0.1 m/s in velocity and 10° in direction, except R2 and R4, which suffer from larger RMSE linked to larger biases (Table 2). The degraded performance of R2 and R4 can be traced back to the larger discrepancies observed with the fitted WASV correction (Figure 6 (left)) for the R2 aft-looking antenna pair (line of sight around 270° in azimuth) and the R4 fore-looking antenna pair (300° in azimuth). This could explain some of the anomalous vectors seen in Figure 8 for R2 and R4. Both R2 and R4 took place at the beginning of the star pattern acquisition and could have experienced slightly different geophysical conditions from those seen during other runs. The availability of NRCS measurements would have helped both retrieval and interpretation by providing information about wind conditions at each point, but these were unfortunately not available due to the lack of system amplitude calibration.

5. Conclusions

This paper presents the first estimation based on data alone of the Wind-wave-induced Artifact Surface Velocity (WASV), which affect SAR and ATI SAR ocean surface velocity data. The findings are based on a comprehensive collection of airborne ATI SAR data over a well-instrumented validation site during the Wavemill proof-of-concept experiment. The results confirm the very strong impact of WASV on SAR Doppler measurements.

For the geophysical conditions encountered during the airborne experiment (wind speed of 5.5 m/s, tidal current of 0.7 m/s, swell $H_s = 0.5$ m, $\lambda = 53$ m), the Doppler shift was dominated by the WASV. The WASV amplitude in the upwind direction reached 1.6 m/s at 27° incidence and 0.9 m/s at 43° incidence, i.e., up to 30% of the wind speed. The star pattern of the airborne campaign offered the perfect means of exploring the azimuth dependence of the wind-wave effects. The results highlight in particular the strong upwind/downwind asymmetry in the magnitude of the WASV, with the upwind value about 1.7 times larger than the value in the downwind direction. There was no evidence of impact by swell, possibly because of the low energy of the swell system during the flights.

The airborne estimates of the WASV show excellent agreement with the estimates reported for spaceborne Envisat ASAR by *Mouche et al*. [2012]. The agreement is remarkable given the differences in frequency (C-band versus X-band), platform (spaceborne versus airborne), instrument (SAR versus ATI SAR), method (global analyses against ECMWF model winds versus local analyses against in situ data), and environmental conditions (e.g., open ocean versus coastal). This work represents the first independent validation of the C-DOP model by *Mouche et al*. [2012], which was derived from globally distributed SAR data over a wide range of ocean conditions.

Our results reveal the very good mapping and current retrieval capabilities of the airborne Wavemill instrument over MBL. After removing the WASV, the Wavemill-retrieved currents show very good agreement with the ADCP measurements, with a root-mean-square error (RMSE) of 0.1 m/s in velocity and 10° in direction for all except two runs (R2 and R4). The anomalies in R2 and R4 are linked to larger biases against the ADCP data of the order of ± 0.2 m/s, which cannot be interpreted in view of the lack of calibrated NRCS data from the airborne instrument.

The Wavemill airborne proof-of-concept data were acquired in atypical geophysical conditions (crossing wind/wave/current; mixed sea with a low-amplitude swell crossing a fetch limited wind-sea; relatively shallow water). Fortunately, the geophysical conditions were very well documented thanks to the comprehensive set of in situ validation data. More airborne experiments are needed in other geophysical conditions,

particularly in the presence of swell, and preferably with an instrument with multiple polarization capability. Further experiments are needed to improve our understanding of these wind and wave effects on SAR Doppler data, and to further develop our ability to quantify and model this important WASV effect at all polarizations and at different spatial scales.

The WASV correction presented in this paper is critical to interpret ocean surface radial velocity from SAR and ATI SAR systems such as Sentinel-1 and TanDEM-X and retrieve accurate ocean surface currents. Once corrected, SAR and ATI SAR can provide measurements of ocean surface currents and winds at high spatial resolution, which are valuable for a wide range of atmospheric and oceanographic issues, including air-sea exchanges, oceanic sub-meso-scale dynamics and oceanic horizontal and vertical transport.

Acknowledgments

The present work was part-funded by European Space Agency contract AO/1-7051/12/NL/AF "Coastal and Ocean Surface Currents Mission Study: Wavemill Product Assessment (WaPA)," with support from the UK Centre for Earth Observation Instrumentation and Space Technology (CEOI-ST) 7th Call "Wavemill Calibration Strategy" award and cofunding from NERC National Capability funding at the National Oceanography Centre. The authors thank Alexis Mouche for the provision of the empirical geophysical model C-DOP, and CEFAS (http://www.cefas.defra.gov.uk/our-science/observing-and-modelling/monitoring-programmes/wavenet.asp) for providing free and open access to the wave spectrum data. The OSCAT (Oceansat-2, ISRO) wind data were obtained from the Physical Oceanography Distributed Active Archive Center (PO.DAAC) at the NASA Jet Propulsion Laboratory, Pasadena, CA (http://podaac.jpl.nasa.gov). We also thank Bertrand Chapron and Meric Srokosz for their helpful comments while discussing the results.

References

Ardhuin, F., L. Marié, N. Rascle, P. Forget, and A. Roland (2009), Observation and estimation of Lagrangian, Stokes, and Eulerian currents induced by wind and waves at the sea surface, *J. Phys. Oceanogr.*, *39*(11), 2820–2838, doi:10.1175/2009JPO4169.1.

Bara, M., R. Scheiber, A. Broquetas, and A. Moreira (2000), Interferometric SAR signal analysis in the presence of squint, *IEEE Trans. Geosci. Remote Sens.*, *38*(5), 2164–2178, doi:10.1109/36.868875.

Buck, C. (2005), An extension to the wide swath ocean altimeter concept, in *Geoscience and Remote Sensing Symposium, 2005. IGARSS '05. Proceedings. 2005 IEEE International*, vol. 8, pp. 5436–5439, IEEE, N. Y., doi:10.1109/IGARSS.2005.1525970.

Chapman, R. D., B. L. Gotwols, and R. E. Sterner (1994), On the statistics of the phase of microwave backscatter from the ocean surface, *J. Geophys. Res.*, *99*(C8), 16,293–16,301, doi:10.1029/94JC01111.

Chapron, B., F. Collard, and F. Ardhuin (2005), Direct measurements of ocean surface velocity from space: Interpretation and validation, *J. Geophys. Res. Oceans*, *110*, C07008, doi:10.1029/2004JC002809.

Farquharson, G., W. Junek, A. Ramanathan, S. Frasier, R. Tessier, D. McLaughlin, M. Sletten, and J. Toporkov (2004), A pod-based dual-beam SAR, *IEEE Geosci. Remote Sens. Lett.*, *1*(2), 62–65, doi:10.1109/LGRS.2004.826553.

Fois, F., P. Hoogeboom, F. Le Chevalier, and A. Stoffelen (2015), An analytical model for the description of the full polarimetric sea surface Doppler signature, *J. Geophys. Res. Oceans*, *120*, 988–1015, doi:10.1002/2014JC010589.

Fornaro, G., E. Sansosti, R. Lanari, and M. Tesauro (2002), Role of processing geometry in SAR raw data focusing, *IEEE Trans. Aerosp. Electron. Syst.*, *38*(2), 441–454, doi:10.1109/TAES.2002.1008978.

Frasier, S., and A. Camps (2001), Dual-beam interferometry for ocean surface current vector mapping, *IEEE Trans. Geosci. Remote Sens.*, *39*(2), 401–414, doi:10.1109/36.905248.

Gelpi, C., and K. Norris (2003), Estimated surface-wave contributions to radar Doppler velocity measurements of the ocean surface, *Remote Sens. Environ.*, *87*(1), 99–110, doi:10.1016/S0034-4257(03)00177-9.

Goldstein, R., and H. Zebker (1987), Interferometric radar measurement of ocean surface currents, *Nature*, *328*, 707–709.

Goldstein, R. M., T. P. Barnett, and H. A. Zebker (1989), Remote sensing of ocean currents, *Science*, *246*(4935), 1282–1285.

Graber, H. C., D. R. Thompson, and R. E. Carande (1996), Ocean surface features and currents measured with synthetic aperture radar interferometry and HF radar, *J. Geophys. Res.*, *101*(C11), 25,813–25,832, doi:10.1029/96JC02241.

Hansen, M., F. Collard, K. Dagestad, J. Johannessen, P. Fabry, and B. Chapron (2011), Retrieval of sea surface range velocities from Envisat ASAR Doppler centroid measurements, *IEEE Trans. Geosci. Remote Sens.*, *49*(10), 3582–3592, doi:10.1109/TGRS.2011.2153864.

Hansen, M., V. Kudryavtsev, B. Chapron, J. Johannessen, F. Collard, K.-F. Dagestad, and A. Mouche (2012), Simulation of radar backscatter and Doppler shifts of wave–current interaction in the presence of strong tidal current, *Remote Sens. Environ.*, *120*, 113–122, doi:10.1016/j.rse.2011.10.033.

Hersbach, H., A. Stoffelen, and S. de Haan (2007), An improved C-band scatterometer ocean geophysical model function: CMOD5, *J. Geophys. Res.*, *112*, C03006, doi:10.1029/2006JC003743.

Hwang, P. A., J. V. Toporkov, M. A. Sletten, D. Lamb, and D. Perkovic (2006), An experimental investigation of wave measurements using a dual-beam interferometer: Gulf stream as a surface wave guide, *J. Geophys. Res.*, *111*, C09014, doi:10.1029/2006JC003482.

Mouche, A., F. Collard, B. Chapron, K. Dagestad, G. Guitton, J. Johannessen, V. Kerbaol, and M. Hansen (2012), On the use of Doppler shift for sea surface wind retrieval from SAR, *IEEE Trans. Geosci. Remote Sens.*, *50*(7), 2901–2909, doi:10.1109/TGRS.2011.2174998.

Mouche, A. A., B. Chapron, N. Reul, and F. Collard (2008), Predicted Doppler shifts induced by ocean surface wave displacements using asymptotic electromagnetic wave scattering theories, *Waves Random Complex Media*, *18*(1), 185–196, doi:10.1080/17455030701564644.

Nouguier, F., C. Guerin, and G. Soriano (2011), Analytical techniques for the Doppler signature of sea surfaces in the microwave regime. II: Nonlinear surfaces, *IEEE Trans. Geosci. Remote Sens.*, *49*(12), 4920–4927, doi:10.1109/TGRS.2011.2153207.

Plant, W. J. (1997), A model for microwave Doppler sea return at high incidence angles: Bragg scattering from bound, tilted waves, *J. Geophys. Res.*, *102*(C9), 21,131–21,146, doi:10.1029/97JC01225.

Plant, W. J., and W. Alpers (1994), An introduction to SAXON-FPN, *J. Geophys. Res.*, *99*(C5), 9699–9703, doi:10.1029/93JC03482.

Röhrs, J., A. Sperrevik, K. Christensen, G. Broström, and Ø. Breivik (2015), Comparison of HF radar measurements with Eulerian and Lagrangian surface currents, *Ocean Dyn.*, *65*(5), 679–690, doi:10.1007/s10236-015-0828-8.

Romeiser, R., and D. Thompson (2000), Numerical study on the along-track interferometric radar imaging mechanism of oceanic surface currents, *IEEE Trans. Geosci. Remote Sens.*, *38*(1), 446–458, doi:10.1109/36.823940.

Romeiser, R., H. Runge, S. Suchandt, R. Kahle, C. Rossi, and P. Bell (2014), Quality assessment of surface current fields from TerrASAR-X and TanDEM-X along-track interferometry and Doppler centroid analysis, *IEEE Trans. Geosci. Remote Sens.*, *52*(5), 2759–2772, doi:10.1109/TGRS.2013.2265659.

Rufenach, C. L., R. A. Shuchman, and D. R. Lyzenga (1983), Interpretation of synthetic aperture radar measurements of ocean currents, *J. Geophys. Res.*, *88*(C3), 1867–1876, doi:10.1029/JC088iC03p01867.

Shemer, L., M. Marom, and D. Markman (1993), Estimates of currents in the nearshore ocean region using interferometric synthetic aperture radar, *J. Geophys. Res.*, *98*(C4), 7001–7010, doi:10.1029/92JC02962.

Shuchman, R. A., and G. A. Meadows (1980), Airborne synthetic aperture radar observation of surf zone conditions, *Geophys. Res. Lett.*, *7*(11), 857–860, doi:10.1029/GL007i011p00857.

Thompson, D. R., B. L. Gotwols, and W. C. Keller (1991), A comparison of Ku-band Doppler measurements at 20° incidence with predictions from a time-dependent scattering model, *J. Geophys. Res.*, *96*(C3), 4947–4955, doi:10.1029/90JC02210.

Toporkov, J., and G. Brown (2000), Numerical simulations of scattering from time-varying, randomly rough surfaces, *IEEE Trans. Geosci. Remote Sens.*, *38*(4), 1616–1625, doi:10.1109/36.851961.

Toporkov, J., D. Perkovic, G. Farquharson, M. Sletten, and S. Frasier (2005), Sea surface velocity vector retrieval using dual-beam interferometry: First demonstration, *IEEE Trans. Geosci. Remote Sens.*, *43*(11), 2494–2502, doi:10.1109/TGRS.2005.848603.

Ulander, L., H. Hellsten, and G. Stenstrom (2003), Synthetic-aperture radar processing using fast factorized back-projection, *IEEE Trans. Aerosp. Electron. Syst.*, *39*(3), 760–776, doi:10.1109/TAES.2003.1238734.

Wavemill PoC Team (2012), Wavemill Proof-of-Concept Final report: A proof-of-concept airborne campaign using an existing X-band interferometric SAR instrument, *Ref: WM-RP-ASU-SY-003 v1*, ESA/ESTEC, Noordwijk, Netherlands.